Winter January, 2011

Dark-current-free petawatt laser-driven wakefield accelerator based on electron self-injection into an expanding plasma bubble

Serguei Y. Kalmykov
Sunghwan A. Yi
Arnaud Beck
Agustin F. Lifschitz
Xavier Davoine, et al.

Dark-current-free petawatt laser-driven wakefield accelerator based on electron self-injection into an expanding plasma bubble

2011 Plasma Phys. Control. Fusion 53 014006

(http://iopscience.iop.org/0741-3335/53/1/014006)

Plasma Phys. Control. Fusion **53** (2011) 014006 (16pp) doi:10.1088/0741-3335/53/1/014006

Dark-current-free petawatt laser-driven wakefield accelerator based on electron self-injection into an expanding plasma bubble

S Y Kalmykov[1,4], S A Yi[1], A Beck[2], A F Lifschitz[3], X Davoine[2], E Lefebvre[2], V Khudik[1], G Shvets[1] and M C Downer[1]

[1] Department of Physics, University of Texas at Austin, One University Station C1500, Austin, TX 78712, USA
[2] CEA, DAM, DIF, Bruyères-le-Châtel, 91297 Arpajon Cedex, France
[3] Laboratoire de Physique des Gaz et des Plasmas, Université Paris XI/CNRS, Bâtiment 210, 91405 Orsay Cedex, France

E-mail: kalmykov@physics.utexas.edu

Received 11 November 2009, in final form 5 April 2010
Published 16 December 2010
Online at stacks.iop.org/PPCF/53/014006

Abstract
A dark-current-free plasma accelerator driven by a short ($\leqslant$150 fs) self-guided petawatt laser pulse is proposed. The accelerator uses two plasma layers, one of which, short and dense, acts as a thin nonlinear lens. It is followed by a long rarefied plasma ($\sim 10^{17}$ electrons cm^{-3}) in which background electrons are trapped and accelerated by a nonlinear laser wakefield. The pulse overfocused by the plasma lens diffracts in low-density plasma as in vacuum and drives in its wake a rapidly expanding electron density bubble. The expanding bubble effectively traps initially quiescent electrons. The trapped charge given by quasi-cylindrical three-dimensional particle-in-cell (PIC) simulations (using the CALDER-Circ code) is $\sim$1.3 nC. When laser diffraction saturates and self-guiding begins, the bubble transforms into a bucket of a weakly nonlinear non-broken plasma wave. Self-injection thus never resumes, and the structure remains free of dark current. The CALDER-Circ modelling predicts a few π mm mrad normalized transverse emittance of electron beam accelerated in the first wake bucket. Test-particle modelling of electron acceleration over 9 cm (using the quasistatic PIC code WAKE) sets the upper limit of energy gain 2.6 GeV with $\sim$2% relative spread.

(Some figures in this article are in colour only in the electronic version)

[4] Author to whom any correspondence should be addressed. Present address: Department of Physics and Astronomy, University of Nebraska, Lincoln, NE 68588-0111, USA.

1. Introduction

Plasma wakefields driven by short ($\tau_L \leqslant 150$ fs) petawatt (PW)-class laser pulses [1–6] can accelerate electrons to gigaelectronvolt energy on top of an optical table [7, 8]. Presently, quasi-monoenergetic electrons in the energy range 150–300 MeV are routinely produced [9–17], and the gigaelectronvolt limit is approached with multi-terawatt lasers [12, 15, 18–20]. New short-pulse PW facilities (such as Texas Petawatt [3] (TPW) and POLARIS [4] lasers) open possibilities beyond the gigaelectronvolt limit [21, 22]. High collimation and low-energy spread of gigaelectronvolts electrons needed for staged acceleration [23] and compact x-ray sources [24–26] require optimization of electron injection in order to identify and eliminate phenomena causing 'dark current' (unwanted electrons trapped by the structure and accelerated to high energy) [27].

The problem of dark current in modern laser wakefield accelerators (LWFAs) is aggravated by the fact that to bypass the technical challenge of external injection they work in the blowout (or 'bubble') regime [28, 29]. Electrons accelerated in this regime are *self-injected* from ambient plasma into a single bucket of a strongly broken, fully electromagnetic plasma wake. The bucket forms when all plasma electrons facing the focused laser pulse are expelled by radiation pressure (while fully stripped ions remain immobile). The charge-separation field attracts bulk electrons to the axis thus forming a cavity devoid of electrons (bubble) that trails with relativistic speed behind the driving laser. This structure has been recently visualized in optical probing experiments [30]. In any transverse cross-section of the bubble, the accelerating gradient is uniform and the focusing gradient is linear in radius [8, 31, 32], which is favourable for emittance preservation. This structure, however, is not dark-current-proof. Uncontrollable variations of shape and size of the laser-driven bubble occur in the course of propagation due to both natural evolution of the driving pulse (focusing, defocusing, temporal compression) [21, 22, 33–37] and imperfections of the plasma target (such as long-scale inhomogeneities in jet targets [38]). The resulting variations of wake potentials trigger self-injection of background electrons [21, 22, 33, 34–38]. Once the bubble size L_b grows by $\sim$1% over a propagation length $\sim 10L_b$, robust self-injection occurs even at very low densities, $n_0 \sim 10^{17}\,\text{cm}^{-3}$ [21, 22, 36], where the Lorentz factor $\gamma_b \sim \omega_0/\omega_{pe}$ associated with ultrarelativistic bubble velocity is of order 100 (here, ω_0 is the laser frequency, $\omega_{pe} = (4\pi e^2 n_0/m_e)^{1/2}$ is the electron plasma frequency, $-|e|$ and m_e are the electron charge and rest mass, respectively). Nonlinear beam loading [39] further aggravates the situation leading to continuous uncontrollable self-injection [19, 20]. As a result, emittance dilution and degradation of electron spectra, such as generation of low-energy tails and multiple high-energy spikes, occur [13, 16, 19, 20, 37].

Conversely, a mildly nonlinear three-dimensional (3D) wake driven by a weakly focused PW pulse in a strongly rarefied plasma ($n_0 \sim 10^{17}\,\text{cm}^{-3}$, or $\omega_{pe}/\omega_0 \sim 0.01$) [7, 40] is immune to dark current. To take advantage of this regime, we propose to enforce self-injection artificially by using a combination of bubble and weakly nonlinear wake in the same accelerator. The aim is to create the bubble *locally*, then let it rapidly expand until it transforms into the first bucket of a conventional periodic 3D wake. The expanding bubble effectively traps electrons, which are further accelerated by the non-broken wake bucket with high collimation and a few per cent energy spread. This kind of wake evolution can be organized in a target that consists of two adjacent plasma layers of different densities. Importantly, in *both* plasmas the incident PW pulse is overcritical for relativistic self-focusing (RSF) [41]. A short dense slab placed at the entrance plays the role of a thin nonlinear plasma lens (NLPL) [42]. RSF and the focusing effect of electron density perturbations [43] impart a converging phase front yet keep the waist of the pulse almost intact. Once the NLPL is optimized by appropriate choice of thickness and electron density, the pulse released from the slab focuses in the low-density plasma without breaking up transversely. An electron density bubble forms in the vicinity of the nonlinear focus, then expands and traps copious electrons as the driving laser pulse diffracts out. Later on, a balance between linear diffraction and focusing nonlinearities is achieved, and the laser pulse with large spot size ($r_{sg} \sim \lambda_p = 2\pi/k_p$, where $k_p = \omega_{pe}/c$) and intensity $I_{sg} \sim 10^{19}\,\mathrm{W\,cm^{-2}}$ self-guides over many centimetres of the rarefied plasma. There it drives a non-broken, dark-current-free plasma wake that accelerates earlier injected electrons.

The proposed layered plasma structure can be organized in a differentially pumped gas cell; plasma is created via optical field ionization. The cell may have two (or more) compartments of adjustable length (from a few millimetres to many centimetres) held at different pressures. The plasma thus consists of several adjacent uniform sections with millimetre length transitions (similar to the segmented capillary approach [44]). The large size of compartments and flexibility in NLPL parameters make the design robust.

The paper is organized as follows. In section 2 we overview the basic experimental configuration of planned TPW experiments [21] in which electron self-injection in longitudinally homogeneous plasmas and reduction of the dark current are difficult to achieve together. This configuration and the layered target design presented in sections 3 and 4 may serve as a reference for future experiments with similar laser systems [4]. In section 3, we introduce the NLPL concept and model the dynamics of nonlinear overfocusing, diffraction and self-guiding of the PW laser pulse using a 3D cylindrically symmetric, fully relativistic, time-averaged particle-in-cell (PIC) code WAKE [45]. The simulations use variables (r, z, ξ), where $r = (x^2 + y^2)^{1/2}$ is the radius, z is the propagation variable and $\xi/c = z/c - t$ is the retarded time. The extended paraxial approximation used in the code enables precise calculation of the pulse group velocity and radiation absorption due to the creation of a plasma wake. It applies when the pulse waist size and length are many laser wavelengths. Self-injection and acceleration of plasma electrons are the subject of section 4. Section 4.1 outlines qualitative physics of electron self-injection in the bubble driven by the diffracting laser pulse (more detailed description can be found elsewhere [35, 36]). WAKE modelling of self-injection and acceleration of test electrons in the quasistatic wake is discussed in section 4.2. Non-quasistatic test particles do not contribute to the electron density and current of the plasma wake in the WAKE modelling. The effect of beam loading which is critically important for the determination of electron energy spread and, in some cases, responsible for saturation of self-injection [39], is thus ignored. To include this effect into the modelling framework in order to make experimentally meaningful predictions we resort to full 3D PIC modelling. Section 4.3 presents full 3D PIC simulations of electron self-injection dynamics via a new quasi-cylindrical code CALDER-Circ [46]. Electron self-injection during bubble expansion, termination of injection and formation of a monoenergetic bunch during bubble stabilization and shrinkage are reproduced in a fully dynamic mode (with the beam loading effect included). The PIC simulations of section 4 prove that the optimized target design yields dark-current-free acceleration of 1.3 nC charge to 2.6 GeV energy with $\sim$2% relative energy spread and less than 8π mm mrad normalized transverse emittance. The conclusion summarizes the results and points out directions for further development. NLPL optimization is presented in the appendix.

2. Self-guiding of PW laser pulse in uniform plasmas

We present here one possible experimental configuration of a PW laser-driven plasma accelerator [4, 21]. A linearly polarized, Gaussian in space and time pulse with central wavelength $\lambda_0 = 1.057\,\mu$m, average power $P = 1.33$ PW and full width at half maximum in intensity $\tau_L = 150$ fs is focused to a spot with radius $r_0 = 80\,\mu$m (at the level exp(−2) of peak intensity) at the foot of a plasma density front ramp. It then propagates in the positive z direction. The vacuum Rayleigh length $Z_{R0} = (\pi/\lambda_0)r_0^2 \approx 1.9$ cm. The initial peak intensity $I_0 = 1.35 \times 10^{19}$ W cm^{-2} corresponds to normalized (to $m_e c^2/|e|$) vector potential $a_0 \approx 3.3$. A fully ionized helium plasma spans from $z = 0$ to 9.5 cm and has a flat-top density profile with linear 1 mm long ramps at the entrance and exit. We model the laser self-guiding over this distance using the code WAKE. The chosen grid size $\Delta\xi = (2/3)\Delta r = 0.05k_p^{-1}$ with 24 macroparticles per radial cell is sufficient to resolve the fine structure of electron bubble.

Given the laser energy, duration and waist size (in the experiment they are prescribed by the amplifier and focusing system), electron density remains the only parameter that controls the nonlinear pulse dynamics. The pulse with $P/P_{cr} \gg 1$ (where $P_{cr} = 16.2\omega_0^2/\omega_{pe}^2$ GW is the RSF critical power [41]) and $\omega_{pe}\tau_L \geqslant \pi$ self-focuses until the charge-separation force of a fully evacuated electron density channel (bubble with a radius L_b) balances the radial ponderomotive force. Once the balance is achieved, the self-guided laser spot size is related to the normalized peak vector potential as $k_p r_{sg} = \alpha a_{sg}^{1/2}$, where $a_{sg} \gg 1$. The value of parameter $\alpha \approx 2r_{sg}/L_b$ depends on the regime of laser–plasma interaction. Simulations show that $1.1 < \alpha < 2$ over a broad range of laser and plasma parameters [8, 47]. Using the expression $P/P_{cr} = a_{sg}^2(k_p r_{sg})^2/32$ based on the fundamental Gaussian representation for the radial profile of the laser pulse [41], we find $a_{sg} = \alpha^{-2/3}2^{5/3}(P/P_{cr})^{1/3}$.

The effect of plasma density on pulse dynamics is examined for $n_0 = 5$, 2.5 and 1×10^{17} cm^{-3}, which correspond to $P/P_{cr} \approx 40$, 20 and 8, respectively. Figure 1(*a*) shows catastrophic consequences of nonlinear focusing in the highest density case, $n_0 = 5 \times 10^{17}$ cm^{-3} ($\omega_{pe}\tau_L \approx 6$). The pulse self-focuses by a factor >20 in intensity within 7 mm ($\approx Z_{R0}/3$), breaks up transversely during defocusing and experiences rapid intensity oscillations during self-guiding. In addition, as shown in figure 1(*b*), nonlinear phase self-modulation and group velocity dispersion, as well as nearly 75% depletion due to the wake excitation, compress the pulse [8, 48] almost to a single cycle around $z = 6$ cm (we stop the simulation soon after this point). The bubble radius in figure 1(*e*) is nearly twice the laser spot size, which gives $\alpha \approx 1$, $a_{sg} \approx 11$ and $I_{sg} \approx 1.5 \times 10^{20}$ W cm^{-2}, in agreement with figure 1(*a*). The bubble is unable to close, which means that the quasistatic approximation fails for nearly all macroparticles making up the bubble sheath. In these circumstances, a non-quasistatic 3D PIC simulation would show continuous electron self-injection.

For $n_0 = 2.5 \times 10^{17}$ cm^{-3} ($\omega_{pe}\tau_L \approx 4.2$), self-focusing is milder, and figure 1(*a*) (red/dark grey curve) shows that intensity increases only by a factor 8.5 after the first 1.2 cm ($\approx 0.63Z_{R0}$). Transverse breakup is not observed, and the pulse self-guides with slowly varying peak intensity and moderate depletion ($\approx$40% over 9.5 cm). The electron density snapshot in figure 1(*f*) shows that $L_b/r_{sg} \approx 4/3$, which gives $\alpha \approx 3/2$, $a_{sg} \approx 6.6$ and $I_{sg} \approx 5.4 \times 10^{19}$ W cm^{-2}, also in agreement with figure 1(*a*). This time, most plasma electrons remain quasistatic, and the electron bubble allows for precise WAKE modelling. However, even modest pulsations of the peak intensity and spot size of the self-guided pulse cause periodic variations of bubble size. Resulting periodic self-injection [21, 22] similar to that observed earlier in plasma channel simulations [34] and in gas-jet experiments [37] leads to degradation of electron spectra.

For $n_0 = 10^{17}$ cm^{-3}, peak intensity varies very steadily despite $P/P_{cr} \approx 8$. The pulse front steepening seen in figure 1(*d*) is insignificant, and energy depletion remains below 5%. From figure 1(*g*), $r_{sg} \approx L_b$, which gives $\alpha \approx 2$ (as in [8]), $a_{sg} = k_p r_{sg} = 4$, $I_{sg} \approx 2 \times 10^{19}$ W cm^{-2}. Not only does the incident pulse appear to be matched for self-guiding ($r_0 \approx 1.175r_{sg}$), it is also much shorter than a plasma period, $\omega_{pe}\tau_L = 2.7$. RSF is thus additionally compensated by nonlinear refraction caused by electron density perturbations [7, 49]. Although the pulse duration is almost resonant for longitudinal wake excitation [50], blowout does not fully

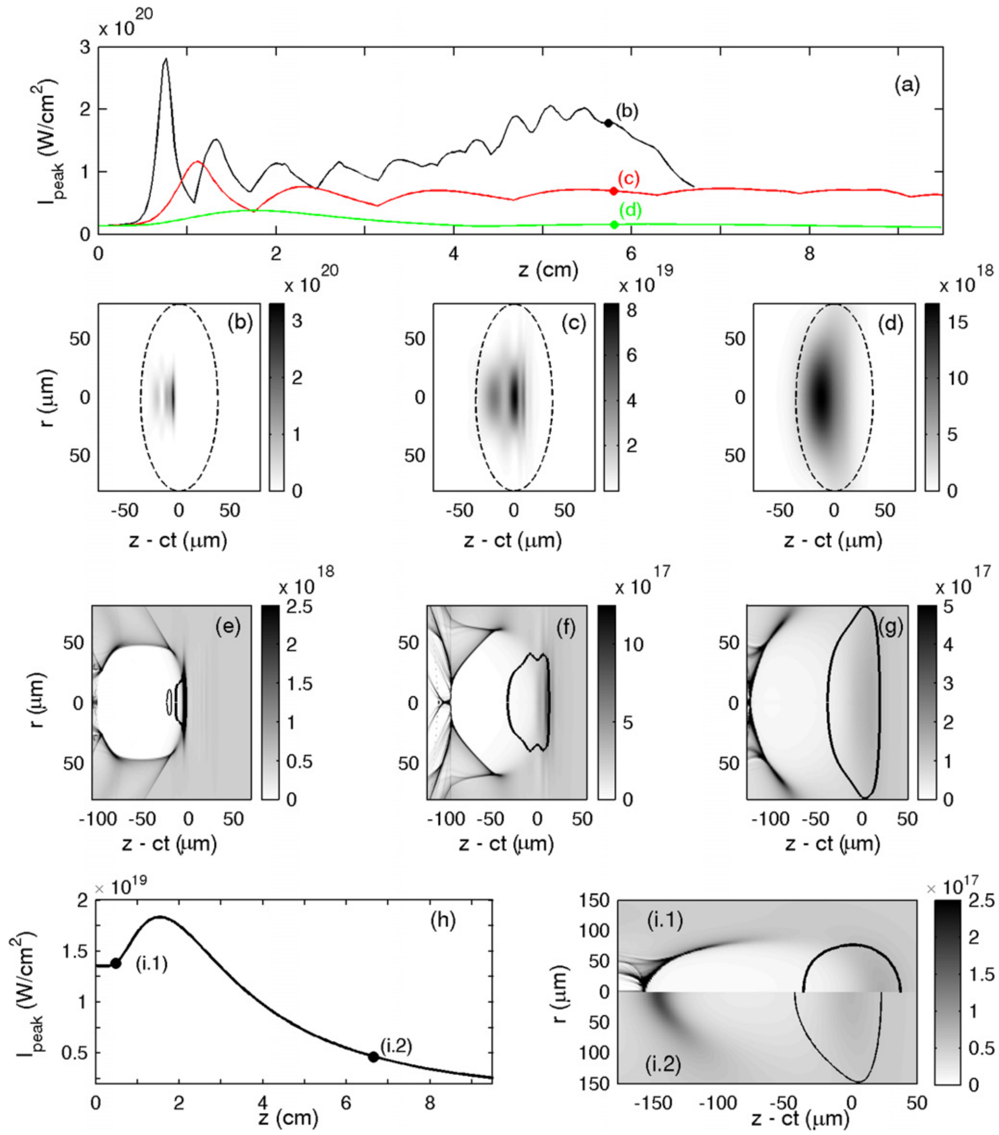

Figure 1. Nonlinear focusing and self-guiding of the 1.33 PW laser pulse. Panel (*a*): peak intensity versus propagation distance for $n_0 = 1$ (green/light grey), 2.5 (red/dark grey) and $5 \times 10^{17}\,\mathrm{cm}^{-3}$ (black). Panels (*b*), (*c*), (*d*): laser intensity in accordingly labelled positions in panel (*a*); dashed line is an iso-contour of laser pulse intensity at $z = 0$ (at $\exp(-2)$ of the peak). Panels (*e*), (*f*), (*g*): first bucket of a plasma wake and laser intensity iso-contours corresponding to panels (*b*), (*c*), (*d*), respectively. Bottom: (*h*) peak intensity versus distance in very low-density plasma, $n_0 = 5 \times 10^{16}\,\mathrm{cm}^{-3}$; (*i*) electron density and intensity iso-contours for appropriately labelled positions in panel (*h*). As the laser diffracts out, the wake becomes non-broken, and the first bucket gradually shrinks. (Colour online.)

develop (the density depression in the first bucket is about 80%). Steady evolution of the first bucket and the absence of complete blowout eliminate the threat of dark current; on the other hand, self-injection becomes problematic and has to be enforced artificially. Further reduction in electron density makes self-guiding inefficient, and the laser pulse diffracts out.

When $n_0 = 5 \times 10^{16}\,\mathrm{cm}^{-3}$, a strong wakefield exists only over the distance $L \approx Z_{R0}$ [7, 49], as is clearly seen in figures 1(h) and (i).

Although dense plasmas ($P/P_{\mathrm{cr}} > 20$, $\omega_{\mathrm{pe}}\tau_{\mathrm{L}} \approx 2\pi$) perform poorly as guiding media, they can effectively focus high-intensity pulses. Focused intensity can be controlled with an appropriate choice of plasma density and length. On the other hand, rarefied plasmas ($P/P_{\mathrm{cr}} < 10$, $\omega_{\mathrm{pe}}\tau_{\mathrm{L}} < 3$) can support the dark-current-free plasma wake over tens of centimetres with steady evolution and negligible laser depletion [7]. In the next section we shall combine the two plasmas in a single target that underlies a robust PW laser-driven dark-current-free LWFA with self-injection.

3. PW laser focusing with a thin NLPL

The target is composed of a short dense ($n_{\mathrm{nlpl}} = 5 \times 10^{17}\,\mathrm{cm}^{-3}$) plasma slab (NLPL) followed by a long uniform plasma of much lower density, $n_{\mathrm{acc}} = 10^{17}\,\mathrm{cm}^{-3}$ (accelerator). The entire plasma length (NLPL and accelerator) is 9.5 cm, as in section 2. The density profile used in simulations is shown in inset (a) of figure 2. Technically, the dense slab may be an embedded gas jet or a front compartment of a differentially pumped cell held at higher pressure. The pulse that traverses the dense plasma acquires a converging phase front imparted by relativistic and ponderomotive focusing nonlinearities [43]. As a result, the pulse focuses into the accelerator plasma producing blowout, then diffracts and drives an expanding bubble that traps copious electrons. As soon as diffraction stabilizes and self-guiding begins, the bubble transforms into a first non-broken bucket of a conventional nonlinear 3D plasma wake, and the electron self-injection ceases. Electrons trapped in the bucket are further accelerated with low energy spread and good collimation. To reduce aberrations, prevent transverse breakup of the pulse and avoid electron self-injection in the first bucket on the density downramp between the NLPL and accelerator plasmas [51], strong focusing and blowout *inside* the NLPL should be avoided (i.e. a thin lens approximation must hold [42]). This requirement limits the NLPL length to [43]

$$L_{\mathrm{nlpl}} < (Z_{R0}/2)(a_0/2)^2(P/P_{\mathrm{cr}})^{-1/2}. \tag{1}$$

For the 1.33 PW pulse of section 2, this condition gives $L_{\mathrm{nlpl}} < 4$ mm, in agreement with WAKE modelling in the appendix. In the simulation presented below, the NLPL has a 4 mm flat-top portion and 1 mm linear ramps on either side (figure 2(a)). Figure 2 shows that the pulse focuses to peak intensity $1.15 \times 10^{20}\,\mathrm{W\,cm}^{-2}$ (spot size 24 μm) in 2.5 mm after NLPL. As shown in the appendix, peak focused intensity and the position of the nonlinear focus are almost unaffected by the presence of low-density accelerator plasma. The NLPL, however, is not free of aberrations, and about 40% of the pulse energy diffracts out of the box.

Comparison of the results of figure 2 with the cases of long uniform dense and rarefied plasmas described in section 2 shows that the design with two-plasma layers uses benefits of both. The peak focused intensity can be as high as for the long dense uniform plasma, and can be properly adjusted (by varying the NLPL thickness) in order not to disrupt subsequent self-guiding over ∼9 cm of low-density (accelerator) plasma. At the same time, the violent laser dynamics typical of dense plasmas is completely avoided. This is the best case scenario for the LWFA because the blowout and electron injection occur only once (in the vicinity of nonlinear focus). The wake then remains mildly nonlinear and non-broken over the entire remaining propagation distance. We shall discuss details of electron injection and acceleration in the following section.

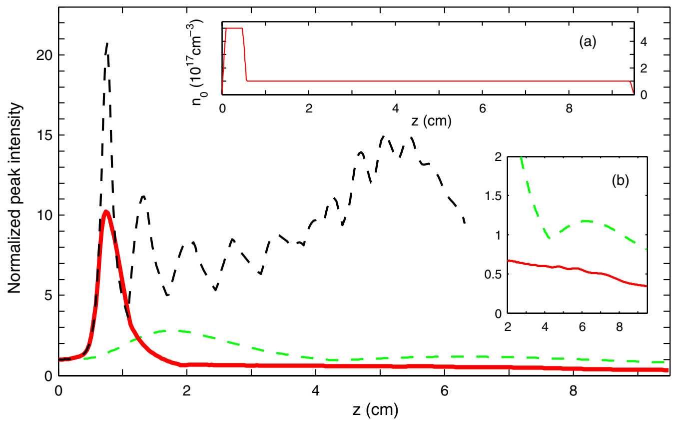

Figure 2. Focusing and self-guiding of 1.33 PW laser pulse in a two-plasma target (density profile shown in inset (*a*)). Black and green/light grey dashed curves correspond to homogeneous plasmas with $n_0 = 5$ and $1 \times 10^{17}\,\mathrm{cm}^{-3}$, respectively. Red/dark grey curve corresponds to the pulse overfocused with an NLPL ($n_{\mathrm{nlpl}} = 5 \times 10^{17}\,\mathrm{cm}^{-3}$) and released for self-guiding into the rarefied accelerator plasma with $n_{\mathrm{acc}} = n_{\mathrm{nlpl}}/5$. Inset (*b*): peak intensity variation of the self-guided laser. Overfocusing does not destroy the pulse, which diffracts and then self-guides with just 40% depletion. (Colour online.)

4. Self-injection of electrons into the expanding plasma bubble and monoenergetic acceleration in dark-current-free LWFA

4.1. Qualitative physics of electron self-injection near nonlinear laser focus

In this and the following subsections, we discuss electron self-injection and acceleration using a test-particle model. The model describes motion of initially quiescent test electrons in the electromagnetic fields of self-consistently evolving quasistatic bubble (obtained from a WAKE simulation). A fully 3D test-particle tracking module built into the WAKE code is fully dynamic, relativistic and non-averaged in time. At each time step, a fresh group of quiescent ($\gamma_{\mathrm{e}} = 1$) test electrons is placed in the simulation box before the laser pulse. The particle tracker accurately describes their interaction with both quasi-paraxial high-frequency laser field (taking into account the linear laser polarization) and slowly varying electric and magnetic fields of the plasma wake [52]. For a given set of laser and plasma parameters, observation of self-injection via test-particle modelling sufficiently motivates subsequent time-consuming massively parallel 3D PIC simulations. Dynamics of electron injection and acceleration during the period of bubble expansion and shrinkage (predicted in test-particle modelling) is reproduced in section 4.3 in a fully dynamic mode, with beam loading [39, 53] taken into account, in a non-quasistatic 3D PIC simulation with the quasi-cylindrical CALDER-Circ code [46].

Once the PW pulse is focused by NLPL to intensity $\sim 10^{20}\,\mathrm{W\,cm^{-2}}$ and spot size $r_{\mathrm{foc}} \approx 1.5k_{\mathrm{p}}^{-1}$ (as in figure 3(*a*)), the radiation pressure expels all electrons facing the pulse. Fully stripped heavy ions, however, remain at rest. The resulting charge-separation field attracts bulk electrons back to the axis. Trajectories of the innermost electrons overshoot. The closed electron density cavity surrounded by a dense shell ('sheath') of relativistic electrons trails behind the driving laser over the positive ion background. Electrons forming the sheath interact with the bubble the longest [36]. When approaching the point of trajectory crossing, they are already pre-accelerated, $\gamma_{\mathrm{e}} = (1 - v_{\mathrm{e}}^2/c^2)^{-1/2} \gg 1$ [54] and, hence, have much

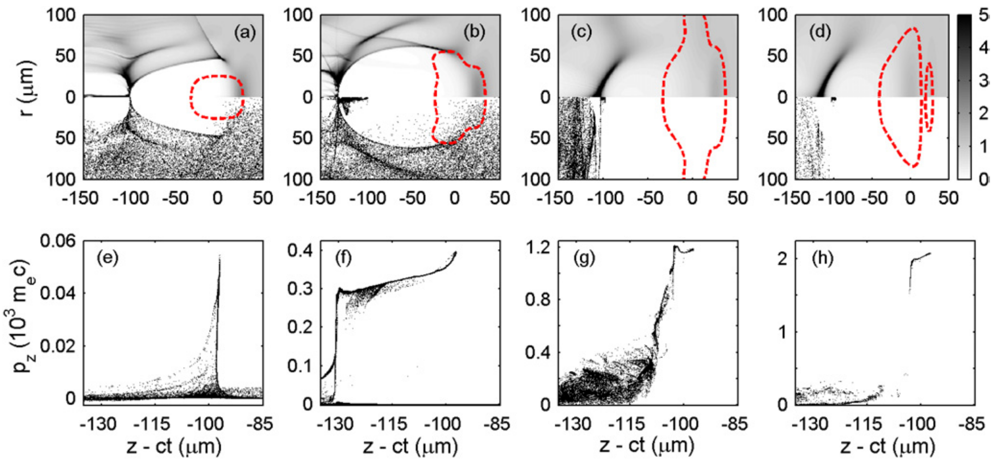

Figure 3. Test electron injection in the expanding bubble and acceleration during the laser self-guiding. Top row—quasistatic electron density in units 10^{17} cm^{-3} (greyscale), the number density of test electrons in (r, ξ) space (dots), and iso-contour of laser intensity (dashed line). Bottom row—corresponding snapshots of longitudinal phase space of test electrons. Snapshots (*a*), (*b*), (*c*) and (*d*) are taken in the positions labelled a, b, c and d in figures 4(*a*) and (*b*). Panels (*a*) and (*e*): bubble and test electrons soon after the nonlinear focus; self-injection begins here. Panels (*b*) and (*f*): the largest possible bubble and the longest electron bunch. Self-injection stops at this point and never resumes. Panels (*c*) and (*g*) correspond to the point where the laser self-guiding begins. First bucket is no longer evacuated. Most of the test electrons are released from the bucket; the remaining particles are further accelerated in the form of compact quasi-monoenergetic bunch. Snapshots (*d*) and (*h*) are taken half-way through the accelerator plasma where the laser is self-guided and first wake bucket remains unchanged. (Colour online.)

higher inertia than the quasistatic electrons of the plasma bulk. As the laser diffracts after the nonlinear focus, the bubble expands and non-quasistatic test electrons get injected, as is clearly seen from a comparison of figures 3(*a*) and (*b*). The injection scenario is akin to trapping a relativistic projectile into the 3D potential bucket as it expands with time. If the bubble expands rapidly enough, some of the heavy sheath electrons lag behind the moving bubble boundary and stay inside the bubble. To trigger this effect, as established in full 3D PIC simulations for a broad range of parameters, the bubble should grow in size by ∼10% over a few tens of bubble lengths [21, 36]. A large fraction of injected electrons become trapped: their moving-frame (MF) Hamiltonian changes from $H_{\mathrm{MF}} = \gamma_{\mathrm{e}} m_{\mathrm{e}} c^2 - |e|\Phi - cP_z = m_{\mathrm{e}} c^2$ before the arrival of the pulse to $H_{\mathrm{MF}} < 0$ (which would be impossible were the laser and bubble non-evolving) [36]; here, Φ is a slowly varying scalar potential and P_z is the longitudinal component of the electron canonical momentum. The quasistatic approximation implies MF Hamiltonian conservation [45]; thus, WAKE macroparticles cannot be trapped.

4.2. Self-injection and acceleration of test electrons in LWFA with NLPL

Figure 3 shows the laser pulse, first wake bucket and test electron phase space after the nonlinear focus and during the guiding stage. Evolution of the laser peak intensity, the length of the first bucket L_{b} (defined as the distance between the first potential maximum and the first minimum on axis) and initial positions and energy spectrum of trapped and accelerated test electrons are displayed in figure 4.

Snapshots (*a*) and (*e*) in figure 3 are taken immediately after the nonlinear focus (position a in figures 4(*a*) and (*b*)). The first wake bucket is a fully evacuated bubble. The bubble expansion

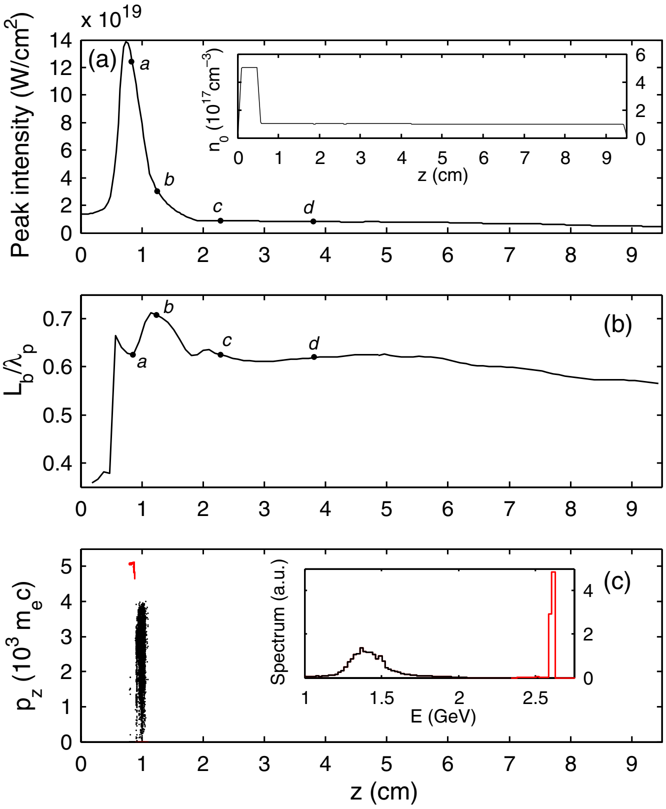

Figure 4. Evolution of (*a*) laser peak intensity and (*b*) first wake bucket length (normalized to λ_p) in the LWFA with a plasma lens. Positions labelled a, b, c and d correspond to panels (*a*), (*b*), (*c*) and (*d*) of figure 3. Inset in panel (*a*): longitudinal profile of electron density. Panel (*c*): longitudinal momentum of test electrons at the exit plane ($z = 9.5$ cm) versus their initial positions. Inset: electron energy spectrum (red/dark grey and black correspond to the electrons from the first and second wake buckets, respectively). Comparison of panels (*a*), (*b*) and (*c*) shows that test electrons are self-injected during the laser defocusing and bubble expansion only. Subsequent shrinkage of the bubble stops the injection; injection never resumes during the self-guided stage. (Colour online.)

has just begun, and signatures of self-injection are not clear yet. As the laser diffracts, the bubble grows and electron self-injection proceeds without interruption. It terminates only when the bubble expansion stops at a distance ≈4.8 mm from the nonlinear focus (position b in figures 4(*a*) and (*b*)). Figure 4(*b*) shows that the bubble length increases by 13.5% over this distance (∼70 bubble lengths). The striking similarity between the number density of test electrons and the quasistatic electron density in figures 3(*a*) and (*b*) shows that the majority of electrons remains quasistatic. Thus, wake evolution can be precisely modelled in a quasistatic framework (a similar situation was tested in [36]).

The bubble is largest and the test electron bunch longest, in figures 3(*b*) and (*f*). After this point, the bubble contracts and stabilizes when the laser pulse becomes self-guided (position c in figures 4(*a*) and (*b*)). Figures 3(*c*) and (*g*) correspond to this point. The first bucket is no longer evacuated, and the wake restores its periodic structure (not shown). Contraction of the first bucket releases a large group of earlier injected electrons; most of them become trapped (with $H_{\rm MF} < 0$) in the second bucket (not shown). All electrons accelerated in the first two buckets have $H_{\rm MF} < m_e c^2$.

Snapshots (*d*) and (*h*) in figure 3 show that the wake bucket changes insignificantly in the course of centimetre-long propagation, which facilitates test electron acceleration in the form of a compact monoenergetic bunch. Finally, as is seen in panel (*c*) of figure 4, the bunch is accelerated to 2.6 GeV energy with a 2.35% energy spread. Normalized transverse emittance of the bunch (i.e. approximate area in the phase space $\boldsymbol{r}_\perp \boldsymbol{p}_\perp$) is $\varepsilon_{N,\perp} = (m_e c)^{-1}(\langle r_\perp^2\rangle\langle p_\perp^2\rangle - \langle \boldsymbol{r}_\perp \boldsymbol{p}_\perp\rangle^2)^{1/2} \approx 1.5\pi$ mm mrad. The electron bunch is concentrated near the axis where the focusing gradient is linear in radius. Therefore, as soon as the phase space of the bunch is filled and the bucket changes slowly, $\varepsilon_{N,\perp}$ is preserved [27]. Thus, the visibly violent injection process does not result in significant emittance dilution.

In this run, test electrons are seeded in the simulation box until the first bucket becomes non-broken ($z \approx 2.1$ cm). Initial positions of test particles reaching the end of the plasma ($z = 9.5$ cm) are plotted in figure 4(*c*). All these particles were trapped during the brief period of laser diffraction and bubble expansion after the nonlinear focus ($0.76 < z < 1.24$ cm), and self-injection never resumed after that. The black dots in figure 4(*c*) show electrons released from the first bucket and trapped and accelerated in the second. Comparison with full 3D PIC modelling described in the next subsection shows that spectacularly strong contraction of the first bucket accompanied by massive release of earlier injected particles is overestimated in quasistatic modelling. Cylindrical beam loading suppresses this effect in full PIC simulation. But even in the worst case scenario copious electrons from the second bucket have average energy twice lower than the energy of the leading bunch, and two orders of magnitude larger emittance (due to ∼10 times higher angular divergence and spot size). Filtering them out experimentally would be a minor technical problem.

4.3. Dynamics of electron self-injection in the quasi-cylindrical 3D PIC simulations

We complement the test-particle study of electron injection and acceleration with a fully dynamic simulation (beam loading included) using the recently developed quasi-cylindrical 3D PIC code CALDER-Circ [46]. This code is highly efficient for the treatment of quasi-paraxial laser propagation in rarefied plasmas because it (a) preserves the realistic geometry of interaction and (b) accounts for the axial asymmetry by decomposing the electromagnetic fields (laser and wake) into a few azimuthal modes (whereas the particles remain in full 3D). Thus, the 3D problem is reduced to an essentially 2D one. Reference [46] shows that in the case of a linearly polarized laser, modes of order $m \geqslant 2$ contribute weakly to the electric field. Our restriction to modes $m = 0$ and $m = 1$ is therefore a very good approximation that allows us to complete the simulation of figure 5 (1.5 cm of propagation) within 32 500 CPU hours (130 h on 250 processors). Resolution in the propagation direction is $\Delta z = 0.125c/\omega_0$ and $\Delta r = 0.4\lambda_0$ is the radial grid size (total number of grid points $12\,000 \times 800 = 9.6 \times 10^6$); 15 particles per cell provide enough accuracy to see both injection and beam loading. The time step is $\Delta t = 0.124\omega_0^{-1}$. Reduced simulation load due to the favourable simulation geometry (well preserved axial symmetry) and reduced description of the radiation beam make it possible to accomplish the quasi-cylindrical PIC modelling within time scales inaccessible to full 3D PIC codes.

The aim of our CALDER-Circ modelling is two-fold. First, as a part of code benchmarking, we validate the dynamical behaviour of laser and bubble observed earlier in the quasi-paraxial, quasistatic WAKE modelling (e.g. features demonstrated in figure 3). Secondly, electron injection and acceleration during the period of bubble expansion and shrinkage (predicted in test-particle modelling with quasistatically evolving bubble) are reproduced

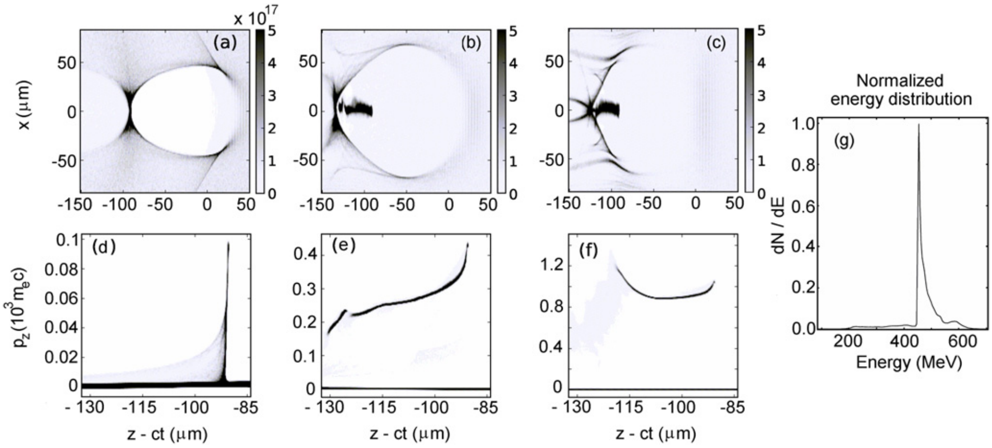

Figure 5. Electron injection into expanding bubble in the quasi-cylindrical CALDER-Circ simulation. Top row: electron density (in units $10^{17}\,\mathrm{cm}^{-3}$) in the plane orthogonal to the laser polarization. Bottom row: corresponding longitudinal momentum distributions. Panels (*a*), (*d*) correspond to the propagation distance $z = 0.83$ mm; electrons with $\gamma > \omega_0/\omega_{pe}$ show up. Panels (*b*), (*e*) correspond to $z = 0.47$ cm; here, the bubble is the largest, and injection stops. Panels (*c*), (*f*) correspond to $z = 1.5$ cm, where the phase space rotation creates a monoenergetic bunch (energy spectrum in plot (*g*)). Panels (*a*), (*b*), (*c*) are direct counterparts of panels (*a*), (*b*), (*c*) of figure 3.

in fully dynamic mode, and with beam loading accounted for; this allows for meaningful predictions of the experimental outcome.

To explore the dynamics of electron injection into the expanding bubble, we start the simulation with a linearly polarized Gaussian pulse focused at the plasma edge. The spot size $r_0 = 24\,\mu$m and peak intensity $1.15 \times 10^{20}\,\mathrm{W\,cm}^{-2}$ correspond exactly to the pulse waist size and intensity in the nonlinear focus from the WAKE simulation of figures 3 and 4. Plasma density profile is flat-top with a 0.3 mm linear front ramp; $n_0 = 10^{17}\,\mathrm{cm}^{-3}$ over the plateau region. This numerical setup is designed to explore the laser defocusing after the nonlinear focus in simulations of figures 3 and 4. Figures 5(*a*)–(*c*) show plasma density, and panels (*d*), (*e*) and (*f*)—the longitudinal phase space of electron bunch. Panel (*g*) displays the electron energy spectrum at the end of the run, $z = 1.5$ cm. In panels 5(*a*) and (*d*), the bubble is shortest, and the signature of self-injection in phase space is just barely seen. These two panels are counterparts of figures 3(*a*) and (*e*). In panels 5(*b*) and (*e*) the bubble is largest, and the electron beam is longest. These panels are counterparts of figures 3(*b*) and (*f*). Panels 5(*c*) and (*f*) correspond to figures 3(*c*) and (*g*) and show the first bucket after the stabilization.

Physical distances between the snapshots 5(*a*), (*b*) and (*c*) from the CALDER-Circ run and between their WAKE counterparts are the same: $\Delta z_{\mathrm{a-b}} \approx 3.87$ mm and $\Delta z_{\mathrm{b-c}} \approx 10.3$ mm. Although dynamics of self-injection is very similar in both simulations, there are obvious differences that can be attributed to the phenomenon of nonlinear beam loading [39, 53]. Comparison of fully self-consistent modelling (figure 5(*b*)) with its quasistatic counterpart (figure 3(*b*)) reveals noticeable distortion of the bubble shape near the rear end. The distortion is produced by transverse fields of the trapped electron bunch [39]. As a consequence, the accelerating gradient reduces, and its longitudinal variation along the bunch becomes less steep. CALDER-Circ macroparticles in the front tip of the bunch are accelerated to the same energy as test electrons in the WAKE code, whereas the rest of the bunch gains on average 20% less energy than test particles. To assess the effect of beam loading we approximate the electron bunch from figure 5(*b*) with a flat-top distribution with a Gaussian radial profile, $n_\mathrm{b}(r) = n_{\mathrm{b}0}\exp(-r^2/\sigma_\mathrm{b}^2)$, where $n_{\mathrm{b}0} = (Q_\mathrm{b}/|e|)(\pi\sigma_\mathrm{b}^2 l_\mathrm{b})^{-1} \approx 2.35\times10^{18}\,\mathrm{cm}^{-3}$ is the peak electron density, $Q_\mathrm{b} \approx 1.5\,\mathrm{nC}$ is the total charge, $\sigma_\mathrm{e} \approx 6\,\mu\mathrm{m}$ is the root-mean-square spot size and $l_\mathrm{b} \approx 35\,\mu\mathrm{m}$ is the length of the bunch. According to [39], the sheath electrons cross the axis, and the bubble remains closed until $R_\mathrm{b}^4/(8r_\mathrm{t}^2\Lambda_0) > 1$, where $\Lambda_0 = \int_0^\infty r(n_\mathrm{b}/n_0)\,\mathrm{d}r = (\sigma_\mathrm{e}^2/2)(n_{\mathrm{b}0}/n_0)$ is the normalized charge per unit length, r_t is the bubble radius in the transverse cross-section taken at the front tip of the bunch and R_b is the bubble radius in the central cross-section. Figure 5(*b*) gives $\Lambda_0 \approx 420\,\mu\mathrm{m}^2$, $r_\mathrm{t} \approx 55\,\mu\mathrm{m}$ and $R_\mathrm{b} \approx 71\,\mu\mathrm{m}$. Hence, $R_\mathrm{b}^4/(8r_\mathrm{t}^2\Lambda_0) \approx 2.5$, and the bubble is not fully loaded. Moreover, CALDER-Circ simulation clearly indicates that injection continues without interruption until the moment of bubble stabilization and ceases only when the contraction begins. Comparison of figures 5(*b*) and (*c*) clearly shows that the transverse fields of the bunch are unable to preclude the bucket contraction; the bubble dynamics and the process of electron self-injection are thus governed primarily by the evolution of the driver rather than by collective fields of trapped electrons. Self-injection never resumes after the point of bubble stabilization, which also agrees with the results of section 4.2.

As is seen in comparison of figures 3(*c*) and 5(*c*), the beam loading prevents strong contraction of the bubble and massive release of trapped electrons into the second bucket (unlike that earlier observed in the quasi-static simulation). However, figures 5(*e*) and (*f*) show that the rear third of the bunch is truncated. Simultaneously, inhomogeneity of the accelerating gradient leads to the phase space rotation: electrons injected later and situated near the base of the bucket are exposed to the higher accelerating force and equalize in energy with the head of the bunch soon after bucket stabilization (this is especially clear from comparison of figures 5(*e*) and (*f*)). The resulting bunch is monoenergetic with the central energy 460 MeV and relative energy spread 1.5% (figure 5(*g*)). This kind of phase space rotation is different from that discussed in [55] and does not require driving the bunch until dephasing. Extrapolation of the obtained results to 7 cm acceleration distance gives $E \sim 2.5\,\mathrm{GeV}$, which agrees with the upper limit set by test-particle modelling. Normalized transverse emittances, $\varepsilon_{N,i} = (m_\mathrm{e}c)^{-1}(\langle x_i^2\rangle\langle p_i^2\rangle + \langle x_i p_i\rangle^2)^{1/2}$, are $\varepsilon_{N,x} = 6.5\pi$ mm mrad and $\varepsilon_{N,y} = 8.2\pi$ mm mrad. As seen in figure 5(*c*), the first wake bucket is no longer an evacuated bubble, hence, self-injection will not resume, and the low relative energy spread and emittance are likely to be preserved.

5. Conclusion

The recently explained mechanism of self-injection of plasma electrons into an expanding electron density bubble [36] is used as the basis for a new dark-current-free design of a PW laser-driven plasma accelerator. The design benefits from focusing properties of dense plasmas and guiding properties of rarefied plasmas. The proposed target consists of two uniform plasmas of different densities with a relatively sharp transition between them. The thin (few millimetres) slab of dense plasma plays the role of a thin nonlinear lens [42]. The relativistic focusing nonlinearity imparts a converging wave front onto the incident PW laser pulse while only moderately perturbing its waist. When released into the low-density plasma, the pulse focuses to intensity $>10^{20}\,\mathrm{W\,cm^{-2}}$ producing full electron blowout near the nonlinear focus before rapidly diffracting. At this stage, the expanding electron density bubble traps copious electrons. In the optimized design, diffraction finally saturates, and the laser pulse self-guides over about 9 cm of rarefied plasma, $n_\mathrm{acc} = 10^{17}\,\mathrm{cm}^{-3}$. It drives a mildly nonlinear plasma wake which accelerates $\sim$1.3 nC charge to the 2.6 GeV energy with a $\sim$2% spread and $<8\pi$ mm mrad normalized transverse emittance. The wake remains non-broken over the

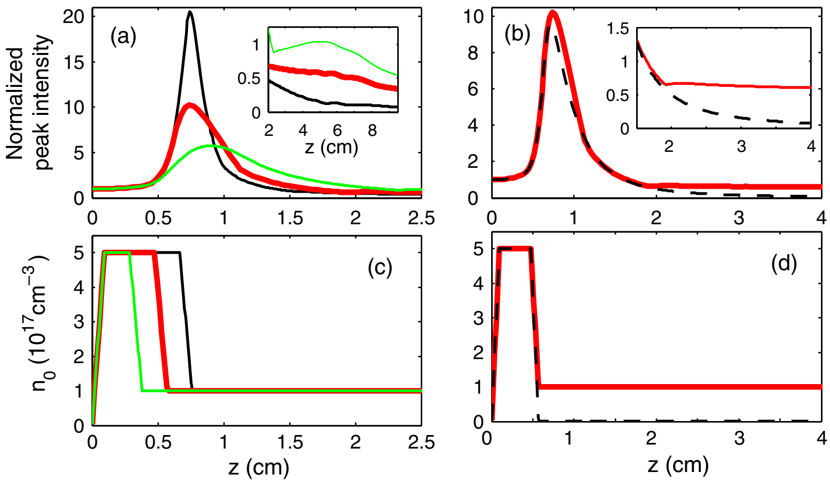

Figure 6. Normalized peak intensity of the laser pulse (*a*), (*b*) and background electron density (*c*), (*d*) versus propagation length. Panels (*a*) and (*c*): focusing properties of the dense plasma slab as a function on its thickness (black: $L_{\mathrm{nlpl}} = 6$ mm, red/dark grey: 4 mm (optimal), green/light grey: 2 mm). Inset: the pulse overfocused with 6 mm slab is poorly guided compared with the optimal case. Panels (*b*) and (*d*): the pulse focusing is weakly affected by the presence of low-density plasma (red/dark grey—two plasmas with $L_{\mathrm{nlpl}} = 4$ mm (optimal case), black dashed—slab followed by vacuum). Inset shows where self-guiding begins in the low-density plasma. (Colour online.)

entire guided stage. Therefore, injection occurs only once (immediately after the nonlinear focus) and dark current is eliminated. Further optimization of the scheme (in combination with a plasma channel [56]) has the potential to meet stringent beam quality requirements of staged acceleration and compact x-ray sources.

Acknowledgments

This work is supported by the US Department of Energy grants DE-FG02-04ER41321, DE-FG02-96ER40954 and DE-FG02-07ER54945. AB and EL acknowledge the support of LASERLAB-EUROPE/LAPTECH through EC FP7 contract no 228334. The authors acknowledge GENCI (www.genci.fr) and the Centre de Calcul pour la Recherche et la Technologie (www-ccrt.cea.fr) at CEA/Bruyère-le-Châtel for providing high performance computing resources that have contributed to the reported research results.

Appendix. Thin NLPL optimization

A 150 fs PW laser pulse (parameters specified in section 2) has to be focused in a low-density accelerator plasma (in our case, $n_{\mathrm{acc}} = 10^{17}\,\mathrm{cm}^{-3}$) to the spot size $r_{\mathrm{foc}} \sim 1.5k_{\mathrm{p}}^{-1} \approx 25\,\mu\mathrm{m}$ and intensity $I_{\mathrm{foc}} > 10^{20}\,\mathrm{W\,cm}^{-2}$. To this end, we use a NLPL—a thin slab of high-density plasma ($n_{\mathrm{nlpl}} \gg n_{\mathrm{acc}}$); n_{nlpl} is such that P/P_{cr} is of the order of a few tens, and plasma period is close to the pulse duration. Nonlinear refraction [43] imparts a converging phase front onto the weakly focused PW pulse, whereas the large spot size $r_0 \approx 80\,\mu\mathrm{m}$ remains almost intact. The NLPL has to be optimized to prevent transverse breakup of the pulse during focusing and achieve stable self-guiding after defocusing.

Longitudinal density profile of the target composed of NLPL and accelerator plasmas is presented in figure 6(*c*). The length $L_{\rm nlpl}$ of the flat-top portion of the NLPL is restricted by condition (1) which excludes laser self-focusing and electron blowout inside the slab. Aberrations are thus reduced, and transverse breakup of the pulse after NLPL is avoided. Density of accelerator plasma is chosen so as to keep $P/P_{\rm cr} < 10$ and pulse duration much shorter than a plasma period. Mutual compensation of relativistic and ponderomotive nonlinearities [7, 49] facilitates vacuum-like focusing (one example is shown in figure 6(*b*)) and increases the pulse stability against the relativistic filamentation [57]. The pulse focuses at a distance $L_{\rm foc}$ from the edge of the NLPL, and then defocuses over roughly the same distance until diffraction and nonlinear focusing compensate each other and self-guiding begins.

WAKE simulations show that $n_{\rm nlpl} = 5 \times 10^{17}\,{\rm cm}^{-3}$ is optimal for focusing the 1.33 PW pulse with the parameters specified in section 2 ($P/P_{\rm cr} = 40$ and $\omega_{\rm pe}\tau_{\rm L} \approx 6$); for these parameters equation (1) gives $L_{\rm nlpl} \leqslant 4\,{\rm mm}$. Importantly, both Raman sidescatter and filamentation [42] remain negligible over this short distance. Once the $n_{\rm nlpl}$ is chosen, $L_{\rm nlpl}$ prescribes the nonlinear focal length $L_{\rm foc}$ and the peak focused intensity $I_{\rm foc}$. Figures 6(*a*) and (*c*) show that 2 mm increments of $L_{\rm nlpl}$ give a factor of 2 increase in $I_{\rm foc}$. $L_{\rm nlpl}$ can be easily controlled with this precision in a differentially pumped cell of adjustable length.

To achieve robust self-injection, not only has full electron blowout to be achieved in the vicinity of nonlinear focus, but the pulse should also rapidly diffract in order to cause ∼10% growth of the bubble size $L_{\rm b}$ over the distance $L_{\rm foc} < 100 L_{\rm b}$. The estimate $L_{\rm b} \approx 0.65\lambda_{\rm p} \approx 70\,\mu{\rm m}$ from figure 4(*b*) sets the upper limit $L_{\rm foc} < 7\,{\rm mm}$. When $L_{\rm nlpl} < 1.5\,{\rm mm}$, this limit is violated. The bubble expands too steadily, and the number of injected electrons drops sharply.

Robust self-injection is achieved with $L_{\rm nlpl}$ in the range 2–4 mm. With $L_{\rm nlpl} = 2\,{\rm mm}$, the NLPL aberrations are weak, and the laser is self-guided with higher intensity than in the case $L_{\rm s} = 4\,{\rm mm}$ (as seen in the inset in figure 6(*a*)). Hence, strongly broken first wake bucket is maintained over almost 7 cm of propagation, and the acceleration proceeds entirely in the bubble regime. Average energy of accelerated test electrons is about 3.7 GeV with the relative spread about 15% and $\varepsilon_{N,\perp} \approx 6.5\pi$ mm mrad.

Increasing $L_{\rm nlpl}$ to 4 mm reduces the focal length $L_{\rm foc}$ from 6 to 2.5 mm and the spot size from $r_{\rm foc} \approx 32.5$ to $24\,\mu{\rm m}$. Focused peak intensity increases from 0.6 to $1.15 \times 10^{20}\,{\rm W\,cm}^{-2}$. Tighter focusing causes stronger aberrations which effectively reduce the laser power (40% of laser energy diffracts out of the interaction region); the transverse beam breakup, however, is not yet the case. Stages of self-injection in the bubble and acceleration in the weakly nonlinear wake become clearly distinguishable. In fact, the first wake bucket remains non-broken after $z \approx 2\,{\rm cm}$, which makes the structure essentially dark-current-free. This best case scenario underpins the subject matter of this paper. Self-injected and accelerated test electrons have the energy 2.6 GeV with 2.35% energy spread and $\varepsilon_{N,\perp} \approx 1.5\pi$ mm mrad.

Further increase in $L_{\rm nlpl}$ results in the laser focusing inside the slab and violation of the thin lens approximation (black curves in figures 6(*a*) and (*c*)). For $L_{\rm nlpl} = 6\,{\rm mm}$ laser focuses to the spot $r_{\rm foc} = 17\,{\rm mm} \approx k_{\rm p}^{-1}$. Filamentation caused by the overfocusing [58] depletes the pulse energy in the interaction region by nearly 80%. Inset in figure 6(*a*) shows that the pulse is not effectively guided. Wakefield is weak, and the mean test electron energy is only 1.1 GeV with the relative spread above 50%.

References

[1] Aoyama M, Yamakawa K, Akahane Y, Ma J, Inoue N, Ueda H and Kiriyama H 2003 *Opt. Lett.* **28** 1594
[2] Hooker C J *et al* 2006 *J. Phys. IV France* **133** 673

[3] Gaul E W *et al* 2010 *Appl. Opt.* **49** 1676
[4] Hein J, Kaluza M C, Bödefeld R, Siebold M, Podleska S and Sauerbrey R 2006 *Lect. Notes Phys.* **694** 47; visit also http://www.physik.uni-jena.de/inst/polaris/
[5] Yanovsky V *et al* 2008 *Opt. Express* **16** 2109
[6] Khazanov E A and Sergeev A M 2008 *Phys.—Usp.* **51** 969
[7] Gorbunov L M, Kalmykov S Y and Mora P 2005 *Phys. Plasmas* **12** 033101
[8] Lu W, Tzoufras M, Joshi C, Tsung F S, Mori W B, Vieira J, Fonseca R A and Silva L O 2007 *Phys. Rev. ST Accel. Beams* **10** 061301
[9] Mangles S P D *et al* 2004 *Nature* **431** 535
[10] Geddes C G R, Toth S, van Tilborg J, Esarey E, Schroeder C B, Bruhwiler D, Nieter C, Cary J and Leemans W P 2004 *Nature* **431** 538
[11] Faure J, Glinec Y, Pukhov A, Kiselev S, Gordienko S, Lefebvre E, Rousseau J P, Burgy F and Malka V 2004 *Nature* **431** 541
[12] Leemans W P, Nagler B, Gonsalves A J, Tóth Cs, Nakamura K, Geddes C G R, Esarey E, Schroeder C B and Hooker S M 2006 *Nature Phys.* **2** 696
[13] Mangles S P D, Thomas A G R, Lungh O, Lindau L, Kaluza M C, Persson A, Wahlström, Krushelnick and Najmudin Z 2007 *Phys. Plasmas* **14** 056702
[14] Maksimchuk A *et al* 2008 *Phys. Plasmas* **15** 056703
[15] Hafz N A M *et al* 2008 *Nat. Photon.* **2** 571
[16] Osterhoff J *et al* 2008 *Phys. Rev. Lett.* **101** 085002
[17] Malka V, Faure J, Rechatin C, Ben-Ismail A, Lim J K, Davoine X and Lefebvre E 2009 *Phys. Plasmas* **16** 056703
[18] Karsch S *et al* 2007 *New J. Phys.* **9** 415
[19] Kneip S *et al* 2009 *Phys. Rev. Lett.* **103** 035002
[20] Froula D *et al* 2009 *Phys. Rev. Lett.* **103** 215006
[21] Kalmykov S Y *et al* 2010 *High Energy Density Phys.* **6** 200–6
[22] Kalmykov S *et al* 2010 *New J. Phys.* **12** 045019
[23] Cheshkov S, Tajima T, Horton W and Yokoya K 2000 *Phys. Rev. ST Accel. Beams* **3** 071301
[24] Rousse A *et al* 2004 *Phys. Rev. Lett.* **93** 135005
[25] Schlenvoight H P *et al* 2008 *Nature Phys.* **4** 130
[26] Grüner F *et al* 2007 *Appl. Phys. B: Lasers Opt.* **86** 431
[27] Rosenzweig J B 2003 *Fundamentals of Beam Physics* (New York: Oxford University Press) p 100
[28] Rosenzweig J B, Breizman B N, Katsouleas T and Su J J 1991 *Phys. Rev.* A **44** R6189
[29] Pukhov A and Meyer-ter-Vehn J 2002 *Appl. Phys. B: Lasers Opt.* **74** 355
[30] Dong P *et al* 2010 *Phys. Rev. Lett.* **104** 134801
Dong P *et al* 2010 *New J. Phys.* **12** 045016
[31] Kostyukov I, Pukhov A and Kiselev S 2004 *Phys. Plasmas* **11** 5256
[32] Lu W, Huang C, Zhou M, Tsoufras M, Tsung F S, Mori W B and Katsouleas T 2006 *Phys. Plasmas* **13** 056709
[33] Xu H, Yu W, Lu P, Senecha V K, He F, Shen B, Qian L, Li R and Xu Z 2005 *Phys. Plasmas* **12** 013105
[34] Oguchi A, Zhidkov A, Takano K, Hotta E, Nemoto K and Nakajima K 2008 *Phys. Plasmas* **15** 043102
[35] Zhidkov A, Fujii T and Nemoto K 2008 *Phys. Rev.* E **78** 036406
[36] Kalmykov S, Yi S A, Khudik V and Shvets G 2009 *Phys. Rev. Lett.* **103** 135004
[37] Hafz N A M, Lee S K, Jeong T M and Lee J 2010 *Nucl. Instrum. Methods in Phys. Res.* A doi:10.1016/j.nima.2010.02.020
[38] Hemker R G, Hafz N M and Uesaka M 2002 *Phys. Rev. ST Accel. Beams* **5** 041301
[39] Tzoufras M, Lu W, Tsung F S, Huang C, Mori W B, Katsouleas T, Vieira J, Fonseca R A and Silva L O 2009 *Phys. Plasmas* **16** 056705
[40] Kalmykov S Y, Gorbunov L M, Mora P and Shvets G 2006 *Phys. Plasmas* **13** 113102
[41] Sun G Z, Ott E, Lee Y C and Guzdar P 1987 *Phys. Fluids* **30** 526
[42] Ren C, Duda B J, Hemker R G, Mori W B, Katsouleas T, Antonsen T M Jr and Mora P 2001 *Phys. Rev.* E **63** 026411
[43] Hafizi B, Ting A, Sprangle P and Hubbard R F 2000 *Phys. Rev.* E **62** 4120
[44] Kaganovich D, Zigler A, Hubbard R F, Sprangle P and Ting A 2001 *Appl. Phys. Lett.* **78** 3175
[45] Mora P and Antonsen T M Jr 1997 *Phys. Plasmas* **4** 217
[46] Lifschitz A F, Davoine X, Lefebvre E, Faure J, Rechatin C and Malka V 2009 *J. Comput. Phys.* **228** 1803
[47] Gordienko S and Pukhov A 2005 *Phys. Plasmas* **12** 043109
[48] Faure J, Glinec Y, Santos J J, Ewald F, Rousseau J P, Kiselev S, Pukhov A, Hosokai T and Malka V 2005 *Phys. Rev. Lett.* **95** 205003
[49] Sprangle P, Esarey E and Ting A 1990 *Phys. Rev.* A **41** 4463

[50] Gorbunov L M and Kirsanov V I 1987 *Sov. Phys.—JETP* **66** 290
[51] Brantov A V, Esirkepov T Zh, Kando M, Kotaki H, Bychenkov V Yu and Bulanov S V 2008 *Phys. Plasmas* **15** 073111
[52] Malka V *et al* 2001 *Phys. Plasmas* **8** 2605
[53] Rechatin C, Davoine X, Lifschitz A, Ben Ismail A, Lim J, Lefebvre E, Faure J and Malka V 2009 *Phys. Rev. Lett.* **103** 194804
[54] Mora P 2009 *Eur. Phys. J. Special Top.* **175** 97
[55] Tsung F S, Narang R, Mori W B, Joshi C, Fonseca R A and Silva L O 2004 *Phys. Rev. Lett.* **93** 185002
[56] Bobrova N A, Bulanov S V, Esaulov A A and Sasorov P V 2000 *Plasma Phys. Rep.* **26** 10
[57] Andreev N E, Gorbunov L M, Mora P and Ramazashvili R R 2007 *Phys. Plasmas* **14** 083104
[58] Thomas A G R *et al* 2007 *Phys. Rev. Lett.* **98** 095004